



# Customizing the anisotropic electronic states of janus-distributive FeN<sub>4</sub> and NiN<sub>4</sub> dual-atom sites for reversible oxygen electrocatalysis

Keying Su<sup>a</sup>, Shan Yang<sup>a</sup>, Anzhou Yang<sup>a</sup>, Yi Guo<sup>a</sup>, Bing Liu<sup>b,\*</sup>, Jiawei Zhu<sup>c,\*</sup>, Yawen Tang<sup>a</sup>, Xiaoyu Qiu<sup>a,\*</sup>

<sup>a</sup> Jiangsu Key Laboratory of New Power Batteries, Jiangsu Collaborative Innovation Center of Biomedical Functional Materials, School of Chemistry and Materials Science, Nanjing Normal University, Nanjing 210023, China

<sup>b</sup> Department of Chemical Engineering, School of Chemical and Material Engineering, Jiangnan University, Wuxi 214122, China

<sup>c</sup> Qingdao Institute of Bioenergy and Bioprocess Technology, Chinese Academy of Sciences, Qingdao 266101, China

## ARTICLE INFO

### Keywords:

Dual-atom catalysts  
Sulfur doping  
Electronic property  
Oxygen electrocatalysis  
Zn-air battery

## ABSTRACT

Non-bonding-type dual-metal atom sites have emerged as a frontier for bifunctional electrocatalysis, however, respectively customizing the local electronic states of two metal sites remains elusive. Herein, by fabricating FeN<sub>4</sub> and NiN<sub>4</sub> single atoms that Janus-distributed on the inner and outer of sulfur-doped carbon hollow spheres, namely FeN<sub>4</sub>-SC-NiN<sub>4</sub>, we demonstrate the sulfur-induced anisotropic electronic regulation for Fe/Ni dual-atom sites and build “one stone two birds” bidirectional facilitation mechanism for reversible oxygen electrocatalysis. For the separated FeN<sub>4</sub> and NiN<sub>4</sub> sites, the ambient sulfur reduces the charges of FeN<sub>4</sub> sites while downshifts the d-band center of NiN<sub>4</sub> sites. Such enlarged difference in electronic structure respectively promotes OH\* desorption at FeN<sub>4</sub> sites but accelerates O<sub>2</sub>\* stripping at NiN<sub>4</sub> sites, enabling the FeN<sub>4</sub>-SC-NiN<sub>4</sub> dual-atom sites to feature simultaneously enhanced oxygen reduction ( $E_{1/2} = 0.844$  V) and oxygen evolution ( $\eta_{10} = 246$  mV<sub>IR-free</sub>) activity, together with a small potential gap (0.632 V) and superior long-term cycling stability for Zn-air battery.

## 1. Introduction

Rechargeable zinc-air battery is a promising renewable device with high theoretical specific energy and economic viability, which involves the oxygen reduction reaction (ORR) and oxygen evolution reaction (OER) as charge and discharge courses at air cathode [1–4]. Deriving from their reversibility, the proton-electron transfer steps of ORR and OER require anisotropic adsorption capacity of oxygen-containing intermediates [5,6]. For ORR ( $O_2 + 2 H_2O + 4e^- \rightarrow 4OH^-$ ), O<sub>2</sub>\* , as a reactant, requires favorable adsorption and low energy barrier for subsequent protonation, while OH\* , as last-step product, requires a weak binding strength for easy desorption [7–9]. Conversely, for OER ( $4OH^- \rightarrow 2 H_2O + O_2 + 4e^-$ ), the O<sub>2</sub>\* in turn as last-step product requires a weak binding strength for facile stripping [10–12]. In an effort to improve the overall output power and meet the compatibility, exploiting bifunctional catalysts to balance the O<sub>2</sub>\* /OH\* adsorption behavior is critical for simultaneously accelerating the kinetics for both ORR and OER [13–16].

Recently, dual-atom catalysts (DACs) without direct bonding have

emerged as a frontier for bifunctional electrocatalysis [17–19]. One side, compared to single-atom catalysts (SACs), selectively integrating two atomic sites together could combine their intrinsic activity to activate the bifunctionality [20–22]. For example, MN<sub>4</sub>-C moieties follow the activity order of Fe > Co > Ni for ORR, and Ni > Co > Fe for OER in alkaline medium, respectively [23–26]. On this basis, the combination of Fe and Ni SACs to form Fe/Ni DACs is promising to break through the activity limitation of individual SACs for bifunctional ORR and OER [27–29]. The other side, compare to directly bonded dual-atom pair, DACs with separately spatial distribution are endowed with more tunability in geometric structure, metal-metal distance, and electronic property, thus could easily optimize the intermediate adsorption configuration and manipulate the reaction pathway [30]. Particularly, a relatively far distance could weaken the interaction between the two metal centers, which is proven to be capable of simultaneously generating two non-interfering metal active sites with different adsorption capacity in one system [31].

Doping alien sulfur atom into the coordination environment of SACs has been widely recognized as a powerful approach to modify their

\* Corresponding authors.

E-mail addresses: [liubing@jiangnan.edu.cn](mailto:liubing@jiangnan.edu.cn) (B. Liu), [zhujw@qibebt.ac.cn](mailto:zhujw@qibebt.ac.cn) (J. Zhu), [07255@njnu.edu.cn](mailto:07255@njnu.edu.cn) (X. Qiu).

<https://doi.org/10.1016/j.apcatb.2023.122694>

Received 12 June 2022; Received in revised form 24 March 2023; Accepted 25 March 2023

Available online 26 March 2023

0926-3373/© 2023 Elsevier B.V. All rights reserved.

electronic structure and enhance the catalytic activity [32–34]. The p-block sulfur with larger atomic radius and lower electronegativity could induce the structural distortion and donate charges to nearby metal centers, tuning the either too strong or too weak adsorption strength of oxygen-containing species [35,36]. However, current sulfur regulation strategy is limited to SACs domain [37], and the role of sulfur on tuning the electronic structure of metal center is single and monotonous. When extending to DACs domain, the electronic role of sulfur (i.e., regulation mechanism, interaction strength, and actuating scope) at two metal sites is still unclear due to distinct chemical properties and multi-component interference in DACs. Moreover, how sulfur doping respectively affects the catalytic activity and selectivity of two metal sites remains to be further elucidated.

Herein, by employing a cheap biomaterial of L-Methionine (L-Met.) as C, N, and S source, we fabricate the FeN<sub>4</sub> and NiN<sub>4</sub> atomic sites that Janus-distributed on the inner and outer of sulfur-doped carbon hollow spheres (denoted as FeN<sub>4</sub>-SC-NiN<sub>4</sub>). X-ray photoelectron spectroscopy (XPS) and X-ray absorption fine structure (XAFS) evidence that the as-formed Fe-N<sub>4</sub> and Ni-N<sub>4</sub> atomic sites are spatially segregated with negligible interaction and not directly bonded with sulfur. Experimentally and theoretically, we demonstrate the anisotropic regulation mechanism of ambient sulfur, which amplifies the difference in electronic structure of FeN<sub>4</sub> and NiN<sub>4</sub> sites and thus enable them to show different selectivity for reversible oxygen electrocatalysis. To be specific, the sulfur dopant reduces the charges for FeN<sub>4</sub> sites but downshifts the d band center for NiN<sub>4</sub> sites, which directionally promotes the OH\* desorption at FeN<sub>4</sub> sites but accelerates the O<sub>2</sub>\* stripping at NiN<sub>4</sub> sites, thus making the ORR more favorable at FeN<sub>4</sub> sites, and so as the OER at NiN<sub>4</sub> sites. Attributed to the “one stone two birds” bidirectional regulation of sulfur, the resultant FeN<sub>4</sub>-SC-NiN<sub>4</sub> dual-atom sites feature both high ORR and OER activity, together with superior long-term cycling stability for Zn-air battery.

## 2. Experimental

### 2.1. Chemicals and materials

The tetraethyl orthosilicate (TEOS), poly(diallyldimethylammonium chloride) (PDDA, Mw < 500,000 Da), hydrofluoric acid (HF) and ferric nitrate nonahydrate (Fe(NO<sub>3</sub>)<sub>3</sub>·9 H<sub>2</sub>O, 99.99%) were purchased from the Sinopharm Chemical Reagent Co., Ltd. (Shanghai, China). The L-Met. and poly(sodium 4-styrenesulfonate) (PSS, Mw < 700,000 Da) were supplied by Shanghai Yuanye Bio-Technology Co., Ltd. The K<sub>2</sub>[Ni(CN)<sub>4</sub>] was purchased from the Alfa Aesar chemical Co., Ltd. The Co(NO<sub>3</sub>)<sub>3</sub>·6 H<sub>2</sub>O was obtained from Shanghai Macklin Biochemical Co., Ltd. The L-His was purchased from Shanghai Ryon Biological Technology Co., Ltd. The commercial Pt/C (20 wt%) and RuO<sub>2</sub> were purchased from Johnson Matthey Chemicals Ltd. (Shanghai, China). All chemicals were used as received without further purification.

### 2.2. Synthesis of FeN<sub>4</sub>-SC-NiN<sub>4</sub>

Firstly, SiO<sub>2</sub> nanospheres with a diameter of 150 nm were prepared via a modified stöber method [38,39]. Then a layer-by-layer assembly approach was served to modify the surface charge distribution of SiO<sub>2</sub> sphere, acquiring the PDPA/PSS/PDPA/PSS-coated SiO<sub>2</sub> with strong-negative charges on the surface. For a typical synthesis of FeN<sub>4</sub>-SC-NiN<sub>4</sub>, 200 mg of Fe(NO<sub>3</sub>)<sub>3</sub>·9 H<sub>2</sub>O, 300 mg of negatively charged SiO<sub>2</sub> nanospheres and 10 mL of deionized water were mixed together and kept continuously sonication for 10 min, forming an uniform suspension. Then the suspension was centrifuged to remove the excess Fe<sup>3+</sup> in the solution, leaving the SiO<sub>2</sub>@Fe<sup>3+</sup> sediment. Afterwards, the SiO<sub>2</sub>@Fe<sup>3+</sup> was re-dispersed in 10 mL of deionized water, adding 300 mg of L-Met (dispersed in 5 mL of deionized water), and kept mechanically stirring for 1 h to obtain the SiO<sub>2</sub>@Fe<sup>3+</sup>@L-Met suspension. Then 120 mg of K<sub>2</sub>[Ni(CN)<sub>4</sub>] was added into above solution and kept stirring

for another 1 h. The resultant mixture was centrifuged to extract the sediment and vacuum-dried at 60 °C to obtain the SiO<sub>2</sub>@Fe<sup>3+</sup>@L-Met@[Ni(CN)<sub>4</sub>]<sup>2-</sup> powder. Then the powder was placed in a porcelain boat and calcined at 700 °C for 3 h under N<sub>2</sub> atmosphere (heating rate: 2 °C min<sup>-1</sup>). At last, the obtained black powder was leached in HF for 1 h to remove the SiO<sub>2</sub> template and washed to neutral to acquire the FeN<sub>4</sub>-SC-NiN<sub>4</sub>.

### 2.3. Synthesis of FeN<sub>4</sub>-C-NiN<sub>4</sub>, mono-component FeN<sub>4</sub>-SC, NiN<sub>4</sub>-SC, S-doped FeNi particles, and S-doped hollow carbon spheres

The FeN<sub>4</sub>-C-NiN<sub>4</sub> dual-atom sites without sulfur doping was prepared by using 150 mg of L-His to substitute 150 mg of L-Met, keeping other experimental conditions consistent with the synthesis of FeN<sub>4</sub>-SC-NiN<sub>4</sub>. Mono-component FeN<sub>4</sub>-SC and NiN<sub>4</sub>-SC single-atom sites were synthesized by only adding the Fe(NO<sub>3</sub>)<sub>3</sub>·9 H<sub>2</sub>O and K<sub>2</sub>[Ni(CN)<sub>4</sub>] as the metal precursor, respectively (see schematic diagram in Fig. S18 and Fig. S19 for details). The S-doped FeNi particles was synthesized by using the standard protocol of FeN<sub>4</sub>-SC-NiN<sub>4</sub>, except for without using SiO<sub>2</sub> template. The S-doped hollow carbon spheres without any metal doping was synthesized by directly calcining and leaching the SiO<sub>2</sub>@L-Met spheres.

### 2.4. Characterizations

Scanning electron microscopy (SEM) images were acquired from Hitachi S4800 at an accelerating voltage of 5 kV. High-resolution transmission electron microscopy (HRTEM) images and energy dispersive X-ray analysis (EDX) were performed on a JEOL JEM-2100 F transmission electron microscope at an accelerating voltage of 200 kV. The aberration corrected high-angle annular dark-field scanning transmission electron microscope (AC-HAADF-STEM) images were performed on JEOL JEM-ARM 200 F. Wide-angle X-ray diffraction (XRD) was performed on a Model D/max-rC X-ray diffractometer with Cu Kα radiation (λ = 0.1541 nm). Brunauer-Emmett-Teller (BET) analysis was measured at 77 K using a Micromeritics ASAP 2050 system. High-resolution XPS was conducted on a Thermo VG Scientific ESCALAB 250 spectrometer with an Al Kα radiator. The binding energy was calibrated by means of the C 1s peak energy of 284.6 eV. XAFS spectra were measured at the beamline BL14W1 station of the Shanghai Synchrotron Radiation Facility, China. The chemical composition of samples was analyzed by inductively coupled plasma atomic emission spectroscopy (ICP-AES). Ultraviolet visible (UV-Vis) spectra was recorded on a Shimadzu UV3600 spectrophotometer with an optical path length of 1 cm at 25 °C. Raman analysis was carried out on a Raman spectrometer (LabRAM HR800, λ = 514 nm).

### 2.5. Electrochemical measurements

All electrochemical measurements were performed on a CHI 760D electrochemical work station (Shanghai Chenhua Co.) at 25 °C. A standard three electrode system was used, including a rotating ring disk electrode (RRDE, 0.196 cm<sup>2</sup>) covered with the catalyst ink as the working electrode, a saturated calomel electrode (SCE) as the reference electrode, and a graphite rod as the auxiliary electrode. All potentials were transformed into RHE by using the conversion formula: E<sub>RHE</sub> = E<sub>SCE</sub> + 0.0591 pH + 0.242. To prepare the working electrode, 2 mg of catalyst, 900 μL of DI water, and 100 μL of Nafion (45 wt%) were ultrasonically dispersed to form a uniform ink. Then 10 μL of the ink was casted onto the glassy carbon electrode and dried at 40 °C. For ORR tests, the polarization curves were obtained using linear sweep voltammetry (LSV) prepared in O<sub>2</sub>-saturated 0.1 M KOH solution at a rotation rate of 1600 rpm and a scan rate of 5 mV s<sup>-1</sup>. For OER tests, the polarization curves were measured in 0.1 M KOH solution recorded from 1.0 to 2.0 V at a scan rate of 5 mV s<sup>-1</sup>. Note that high-purity O<sub>2</sub> was bubbled through the electrolyte during the testing to fix the reversible

oxygen potential. To avoid the peeling of catalyst caused by evolved O<sub>2</sub> adhesion, a rotation speed of 1600 rpm was offered during the OER. The long-term stability tests of ORR and OER were performed by chronoamperometry and accelerated durability tests (ADTs).

## 2.6. Zn-air battery tests

The Zn-air battery measurements were tested in homemade Zn-air cells. The air cathode includes the hydrophilic carbon paper with a catalyst layer on the electrolyte-facing side and a gas-diffusion layer on the air-facing side. The catalyst layer was prepared by loading 10 mg catalyst ink into a 1.0 cm<sup>2</sup> carbon paper. The gas diffusion layer allows O<sub>2</sub> to permeate from the ambient air to the catalyst sites. Zn plate was polished with a thickness of 0.3 mm, then used as the anode. The electrolyte was made of 0.2 M ZnCl<sub>2</sub> + 6 M KOH mixed solution. The cycling stability test was carried out in a Land CT2001A system with 5 min rest time between each discharge and charge at a current density of 5 mA cm<sup>-2</sup>. Each discharge and charge period was set to be 20 min.

## 2.7. Calculation details

All the spin-polarized density functional theory (DFT) calculations were performed by using the Vienna ab-initio simulation package (VASP) [40,41]. The generalized gradient approximation (GGA) with the Perdew-Burke-Ernzerhof (PBE) functional was used to model electronic exchange and correlation [42]. The projector-augmented wave (PAW) method was used to represent core-valence interactions [43]. Valence electrons were described by a plane wave basis with an energy cutoff of 400 eV. Electron smearing was employed through Gaussian smearing method with a smearing width of 0.05 eV. The convergence criteria for force and energy were set to 0.03 eV/Å and 10<sup>-5</sup> eV, respectively. 3 × 3 × 1 k-point mesh was employed for the integration of the Brillouin zone. The van der Waals (vdW) interactions were taken into account when calculating the reaction energetics by using the DFT-D3 approach.

A 5 × 5 supercell graphene slab with four atomic layers consisting of 200 carbon atoms was employed in this work. The Janus-distributed FeN<sub>4</sub>-C-NiN<sub>4</sub> structure was modeled by embedding FeN<sub>4</sub> group into top graphene layer and NiN<sub>4</sub> group into bottom graphene layer. On the basis of FeN<sub>4</sub>-C-NiN<sub>4</sub> structure, the Janus-distributed FeN<sub>4</sub>-SC-NiN<sub>4</sub> structure was modeled by doping S atoms into middle two graphene layers. A 20 Å vacuum gap perpendicular to the surface was added to separate the neighboring slabs in z-direction. All the atoms were allowed to relax during geometric optimization.

The Gibbs free energy for gaseous species was calculated according to Eq. (1):

$$G = E_{DFT} + E_{ZPE} + [H(T, P^\theta) - H(0K, P^\theta)] - T[S(T, P^\theta) - S(0K, P^\theta)] + k_B T \ln \frac{P}{P^\theta} \quad (1)$$

The Gibbs free energy for surface adsorbed species was calculated according to the following equations:

$$G = E_{DFT} + E_{ZPE} + U^o - TS \quad (2)$$

$$U^o = k_B T \sum_i \frac{h\nu_i/k_B T}{e^{h\nu_i/k_B T} - 1} \quad (3)$$

$$S = k_B \sum_i \left[ \frac{h\nu_i/k_B T}{e^{h\nu_i/k_B T} - 1} - \ln(1 - e^{-h\nu_i/k_B T}) \right] \quad (4)$$

where  $E_{DFT}$  and  $E_{ZPE}$  are DFT-calculated energy and zero-point energy, respectively, enthalpy  $H(T, P^\theta)$  and entropy  $S(T, P^\theta)$  of gaseous molecule were obtained from the JANAF thermochemical tables [44],  $P$  is the partial pressure of gaseous molecule,  $P^\theta$  is the standard pressure (100 kPa),  $k_B$  is the Boltzmann constant,  $h$  is the Planck constant,  $T$  represents the Kelvin temperature, and  $\nu_i$  is the vibrational frequency.

## 3. Results and discussion

### 3.1. The role of sulfur for FeN<sub>4</sub> and NiN<sub>4</sub> sites

DFT simulations were first carried out to theoretically unveil the role of sulfur on tuning the electronic states of dual-atom sites. Two structural models, namely FeN<sub>4</sub>-SC-NiN<sub>4</sub> and FeN<sub>4</sub>-C-NiN<sub>4</sub> were built, and a 20 Å vacuum gap perpendicular to the surface was used to separate the neighboring slabs in z-direction, in an effort to rule out the interaction between FeN<sub>4</sub> and NiN<sub>4</sub> sites (Fig. 1a). The charge density isosurfaces show the electron distributions in FeN<sub>4</sub>-SC-NiN<sub>4</sub> and FeN<sub>4</sub>-C-NiN<sub>4</sub> (Fig. 1b). Obviously, the electron density around Ni center is much higher than that around Fe, as marked by red arrows, while the value of Bader charge is opposite. Quantitatively, the Bader charge follows the order of FeN<sub>4</sub>-C (+1.28|e|) > FeN<sub>4</sub>-S doped C (+1.24|e|) > NiN<sub>4</sub>-C (+1.03|e|) > NiN<sub>4</sub>-S doped C (+1.02|e|). Obviously, the introduction of sulfur significantly reduces the Bader charge of Fe site but have a negligible influence on the Bader charge of Ni site, as summarized in Fig. 1c (left). The density of state (DOS) in Fig. 1d show that the d-band center of FeN<sub>4</sub> site is closer to the Fermi level than that of NiN<sub>4</sub> site, whether sulfur doping or not. After sulfur doping, the d-band center of NiN<sub>4</sub> site shows a stronger downward shifting from -1.89 eV to -2.13 eV, while the d-band center of FeN<sub>4</sub> site exhibits a slight shift from -0.33 eV to -0.50 eV, as summarized in Fig. 1c (right). Overall, the introduction of sulfur induces different electronic regulation mechanism for FeN<sub>4</sub> and NiN<sub>4</sub>, which mainly reduces the charge state of FeN<sub>4</sub> sites but downshifts the d-band center of NiN<sub>4</sub>. According to valence-bond and d-band model theory [45], such anisotropic tuning in electronic structure could severally change the binding ability towards different oxygen-containing intermediates, giving opportunity for enhancing the oxygen catalytic selectivity at FeN<sub>4</sub> and NiN<sub>4</sub> sites.

### 3.2. Synthesis and structural characterization of FeN<sub>4</sub>-SC-NiN<sub>4</sub>

In order to put above theoretical models into practice, the FeN<sub>4</sub>-SC-NiN<sub>4</sub> was synthesized by a layer-by-layer space-confinement strategy, using the cheap and sustainable L-Met biomaterial (detailed structure shown in Fig. S1) as N, S, and C source. Fig. 2a displays the synthetic diagram of FeN<sub>4</sub>-SC-NiN<sub>4</sub>, which involves the progressive assembly of negatively charged SiO<sub>2</sub>, SiO<sub>2</sub>@Fe<sup>3+</sup>, SiO<sub>2</sub>@Fe<sup>3+</sup>@L-Met, and SiO<sub>2</sub>@Fe<sup>3+</sup>@L-Met@[Ni(CN)<sub>4</sub>]<sup>2-</sup> (as confirmed by TEM images and EDX mapping in Fig. S2). Then the SiO<sub>2</sub>@Fe<sup>3+</sup>@L-Met@[Ni(CN)<sub>4</sub>]<sup>2-</sup> powders were underwent pyrolysis and leaching to acquire the FeN<sub>4</sub>-SC-NiN<sub>4</sub>. Specifically, the use of L-Met could provide -NH<sub>2</sub> with lone pairs of electrons to strongly bind with Fe<sup>3+</sup> via coordination interactions (as confirmed by UV-vis in Fig. S3), resulting in the formation of Fe single-atoms. Moreover, excess L-Met could further wrap on the SiO<sub>2</sub> surface to segregate the Fe<sup>3+</sup> with other metal precursors, providing foundation for the formation of non-bonding dual-metal sites. The use of [Ni(CN)<sub>4</sub>]<sup>2-</sup> was responsible for the formation of Ni single-atoms, that the cyano groups could disperse the central Ni<sup>2+</sup> to avoid the aggregation after pyrolysis [12]. The structural change at each step was examined by SEM images, which indicates the progressively roughened surface during layer-by-layer adsorption, accompanied by the gradual color change from white, yellow, to dark orange (Fig. S4).

The purity of FeN<sub>4</sub>-SC-NiN<sub>4</sub> was investigated by XRD (Fig. 2b). Two characteristic carbon (002) and (100) diffractions located at 24.8° and 43.0° were observed, and no obvious signals ascribed to Fe or Ni derivatives could be detected, demonstrating the absence of crystalline species. Raman spectra shows the I<sub>D</sub>/I<sub>G</sub> value of 1.02, indicating the well graphitization degree of FeN<sub>4</sub>-SC-NiN<sub>4</sub> (Fig. S5). HRTEM images (Fig. S6) and AC-HAADF-STEM (Fig. 2c) show the structural integrity of FeN<sub>4</sub>-SC-NiN<sub>4</sub>. After removing SiO<sub>2</sub>, the hollow spheres with diameter of 150 nm and shell thickness of 3.5 nm could be well maintained, which interconnected together to form a three-dimensional network structure. Meanwhile, no visible clusters or nanoparticles could be



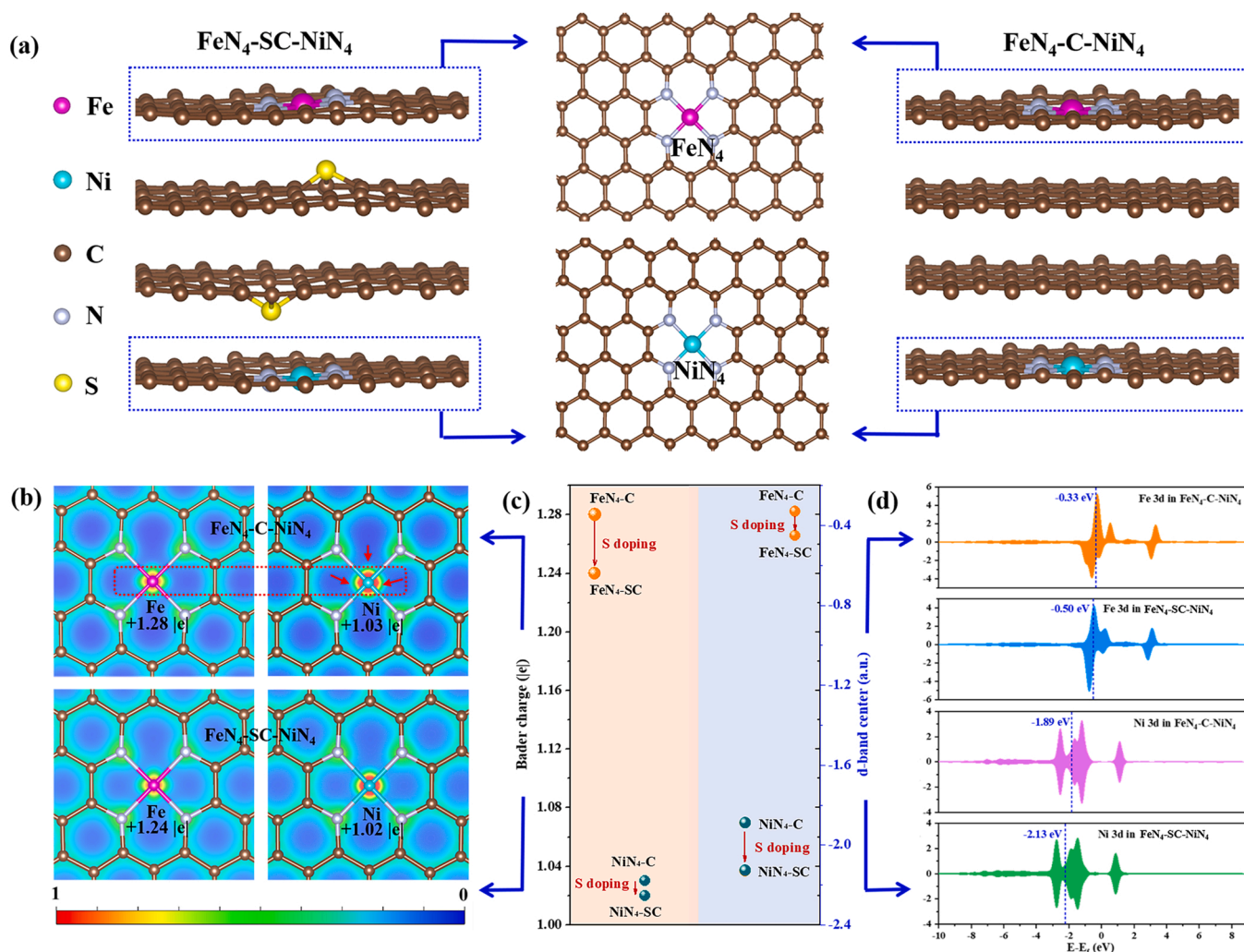


**Fig. 1.** Comparison of the electronic structures of  $\text{FeN}_4\text{-SC-NiN}_4$  and  $\text{FeN}_4\text{-C-NiN}_4$ . (a) Structural models. (b) Charge density isosurfaces. Red and blue color represents a higher and lower electron density, respectively. (c) Trend of Bader charge and d-band center after S doping. (d) DOS for Fe 3d and Ni 3d orbitals.

observed, implying that both the Fe and Ni present atomic dispersion form. The  $\text{N}_2$  adsorption-desorption isotherms show a type-IV hysteresis loop related to mesoporous characteristics, and the Brunauer-Emmett-Teller surface area was determined to be  $131.69 \text{ m}^2 \text{ g}^{-1}$  (Fig. S7). Locally amplified AC-HAADF-STEM indicates the atomic dispersion of Fe and Ni sites, showing a number of randomly dispersed bright dots with size of  $2.0 \text{ \AA}$ , indicative the isolated feature of Fe and Ni atoms and no Fe-Ni dual-atom pairs are formed (Fig. 2d). EDX mapping reveals the spatial distribution of Fe, Ni, C, N, and S elements throughout the entire hollow carbon architecture (Fig. 2e), verifying the well presentation of Fe and Ni sites and successful doping of sulfur. ICP-AES determines that the exact Fe and Ni content in the  $\text{FeN}_4\text{-SC-NiN}_4$  is 0.98 at% and 1.02 at%, respectively. For comparison,  $\text{FeN}_4\text{-C-NiN}_4$  dual-atom sites without sulfur doping was synthesized by using L-His to eliminate the S source. As shown in Fig. S8 and Fig. 2f-g, XRD pattern, HRTEM, HAADF-STEM, and EDX mappings confirm the formation of  $\text{FeN}_4\text{-C-NiN}_4$ .

XPS analysis was conducted to investigate the chemical states in  $\text{FeN}_4\text{-SC-NiN}_4$ . As the full-range XPS survey in Fig. S9, clear signals assignable to Fe, Ni, S, C, N could be well detected, and their contents are listed in Table S1, with C (87.47 at%), N (8.26 at%), S (2.19%), Fe (1.06%), and Ni (1.02%). The Fe 2p and Ni 2p spectra of  $\text{FeN}_4\text{-SC-NiN}_4$  shows main peaks for  $\text{Fe}^{2+}$  (711.7 and 725.1 eV),  $\text{Fe}^{3+}$  (717.1 and 728.0 eV), and  $\text{Ni}^{2+}$  (855.3 and 873.1 eV), respectively [46–48], suggesting the oxidation states of metal species rather than metallic states. The S 2p spectra shows two main peaks located at 163.8 and 165.0 eV,

corresponding to the S  $2p_{3/2}$  and  $2p_{1/2}$  states of thiophene-like structures (C-S-C) [49]. A small peak located at around 168.4 eV refers to the sulfate species. Meanwhile, no metal-sulfur bonding could be detected in S 2p spectra, indicating that sulfur is only incorporated into the hollow carbon spheres [50,51]. The N 1s spectra shows four main peaks at 398.2, 399.6, 400.9, and 403.1 eV, corresponding to the pyridinic-N (40.6%) or metal-N, pyrrolic-N (28.7%), graphitic-N (25.6%), and oxidized-N (5.1%), respectively [52]. The high content of graphitic-N species is favorable for a faster electron transfer for boosting the electrocatalytic kinetics [53]. The high-resolution C 1s spectrum exhibits four peaks at 289.5, 287.4, 285.8, and 284.6 eV, assigned to C=O, C-O or C-S, C-N, and C-C group, respectively [47]. In an effort to shed lights on the variation of electronic structure induced by sulfur, the XPS survey of  $\text{FeN}_4\text{-C-NiN}_4$  was in comparison with the  $\text{FeN}_4\text{-SC-NiN}_4$  (Fig. S10). Both the Fe 2p and Ni 2p of  $\text{FeN}_4\text{-SC-NiN}_4$  show obvious downshifts of 0.5 and 0.3 eV compare to those of the  $\text{FeN}_4\text{-C-NiN}_4$ , indicating the role of ambient sulfur as electron donor to simultaneously donate electrons for FeN<sub>4</sub> and NiN<sub>4</sub> sites (Fig. 3a) [54].

XAFS measurements were performed to analysis the precise coordination of  $\text{FeN}_4\text{-SC-NiN}_4$  (Fig. S11), in comparison with the  $\text{FeN}_4\text{-C-NiN}_4$ , sulfide, foil, and oxide. As the pre-edge peak shown in Fig. 3b, the Fe K edge of  $\text{FeN}_4\text{-SC-NiN}_4$  is upshifted to higher energy region compare to the FeO, Fe<sub>2</sub>S and Fe foil, elucidating that the oxidation state of Fe in  $\text{FeN}_4\text{-SC-NiN}_4$  is near +3. The pre-edge peak for Ni K-edge is situated near NiO and upshifted to higher energy region compare to the Ni<sub>2</sub>S and



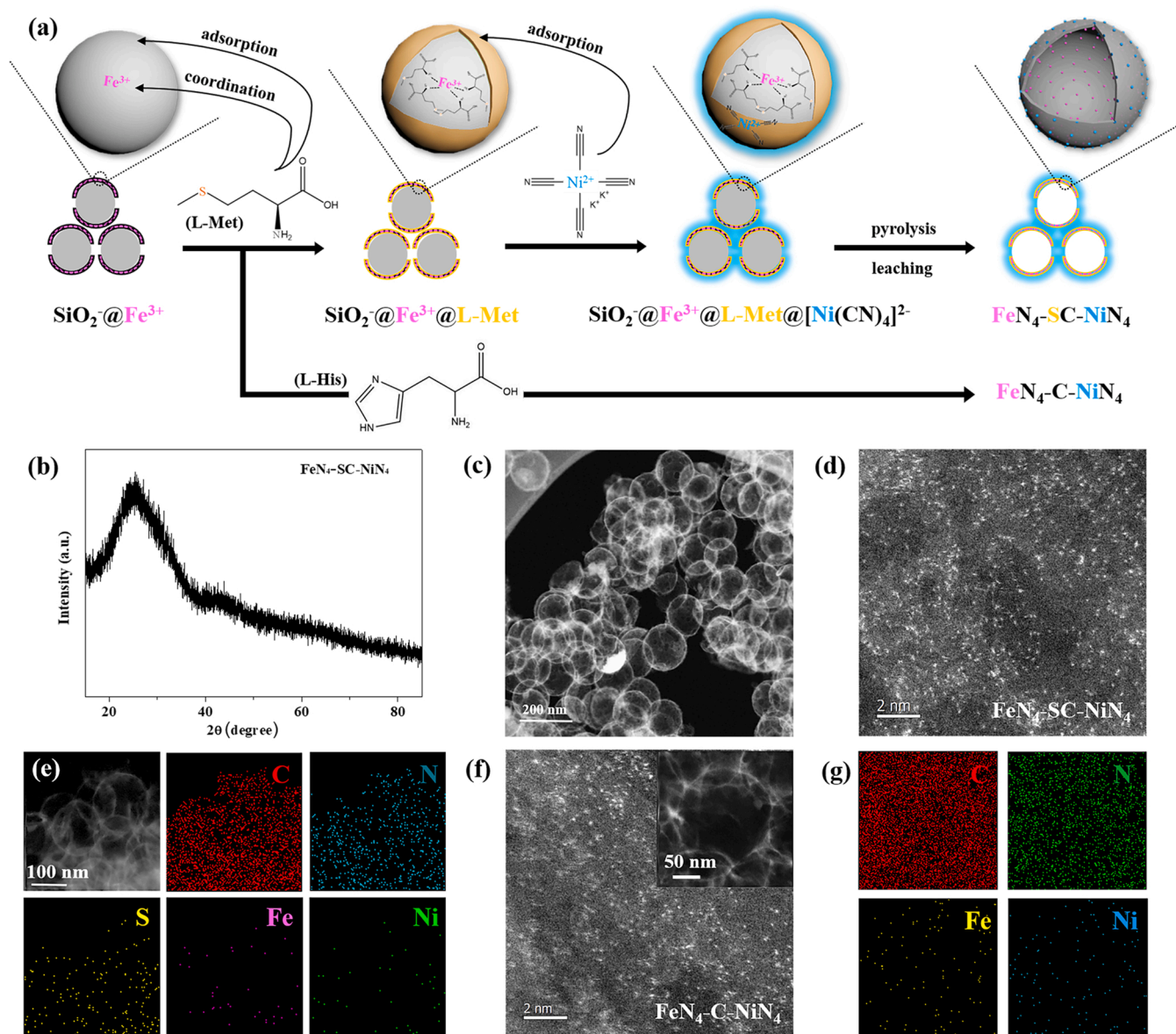


**Fig. 2.** Characteristics of the FeN<sub>4</sub>-SC-NiN<sub>4</sub> and FeN<sub>4</sub>-C-NiN<sub>4</sub>. (a) Synthetic diagram. (b) XRD pattern, (c, d) AC-HAADF-STEM images, and (e) EDX mappings of the FeN<sub>4</sub>-SC-NiN<sub>4</sub>. (f) AC-HAADF-STEM image and (g) EDX mappings of the FeN<sub>4</sub>-C-NiN<sub>4</sub>.

Ni foil, demonstrating the average oxidation state of Ni in FeN<sub>4</sub>-SC-NiN<sub>4</sub> is near + 2 (Fig. 3c). Moreover, both the Fe K-edge and Ni K-edge XANES spectra of FeN<sub>4</sub>-SC-NiN<sub>4</sub> show a bit lower absorption edges than FeN<sub>4</sub>-C-NiN<sub>4</sub>, as locally amplified regions inserted in Figs. 3b and 3c. This is in line with the XPS analysis, further suggesting the role of sulfur as electron donor to decrease the valence of both Fe and Ni. Fig. 3d-e shows the Fourier transform (FT) curves for Fe and Ni K-edge of FeN<sub>4</sub>-SC-NiN<sub>4</sub>. The Fe moiety only presents Fe-N coordination with the peak located at 1.42 Å, meanwhile no related peak corresponding to Fe-Fe, Fe-S, or Fe-Ni could be detected, indicating the exact Fe-N coordination. The Ni moiety shows a sole peak located at 1.41 Å, attributed to the scattering of Ni-N first-shell coordination. Moreover, in comparison with FeN<sub>4</sub>-C-NiN<sub>4</sub>, both the main FT peak for Fe and Ni in FeN<sub>4</sub>-SC-NiN<sub>4</sub> show slightly negative shifts, as marked by short dashes in Figs. 3d and 3e, indicating the atomic configuration tuning induced by sulfur. Through quantitative EXAFS fitting (parameters listed in Fig. S12-S13 and Table S2-S3), the coordination numbers for Fe-N and Ni-N determined by best-fitted results were 4.3 and 3.8, respectively. Thus a probable atomic model could

be constructed, including non-bonding FeN<sub>4</sub> sites, NiN<sub>4</sub> sites, and ambient sulfur. Moreover, the bond length of both Fe-N (2.04 Å) and Ni-N (2.01 Å) in FeN<sub>4</sub>-SC-NiN<sub>4</sub> is slightly shorter than those in FeN<sub>4</sub>-C-NiN<sub>4</sub> (2.08 Å, 2.06 Å), indicating that both the atomic environment at FeN<sub>4</sub> and NiN<sub>4</sub> sites are restructured by ambient sulfur although the Fe-S and Ni-S bonding are not formed. Furthermore, the coordination informations in the second shell are provided to further understand the binding condition of S. For Fe k-edge, both the FeN<sub>4</sub>-SC-NiN<sub>4</sub> and FeN<sub>4</sub>-C-NiN<sub>4</sub> exhibit a small peak locates at 2.45 Å, which could be ascribed to Fe-N-C, or defined as Fe-C second shell coordination. For Ni k-edge, both the FeN<sub>4</sub>-SC-NiN<sub>4</sub> and FeN<sub>4</sub>-C-NiN<sub>4</sub> exhibit a small peak locates at 3.10 Å, which could be ascribed to Ni-N-C, or defined as Ni-C second shell coordination, indicating that S is also not bonded with Fe and Ni site in the second shell. The electronic role of sulfur was also confirmed by wavelet transform (WT) analysis (Fig. S14-S15). Both the FeN<sub>4</sub>-SC-NiN<sub>4</sub> and FeN<sub>4</sub>-C-NiN<sub>4</sub> exhibit only one intensity maximum ascribed to Fe-N and Ni-N contributions, respectively, without the detection of Fe-Fe, Fe-S, Ni-Ni, Ni-S, or Ni-Fe coordination (Fig. S16 and S17).

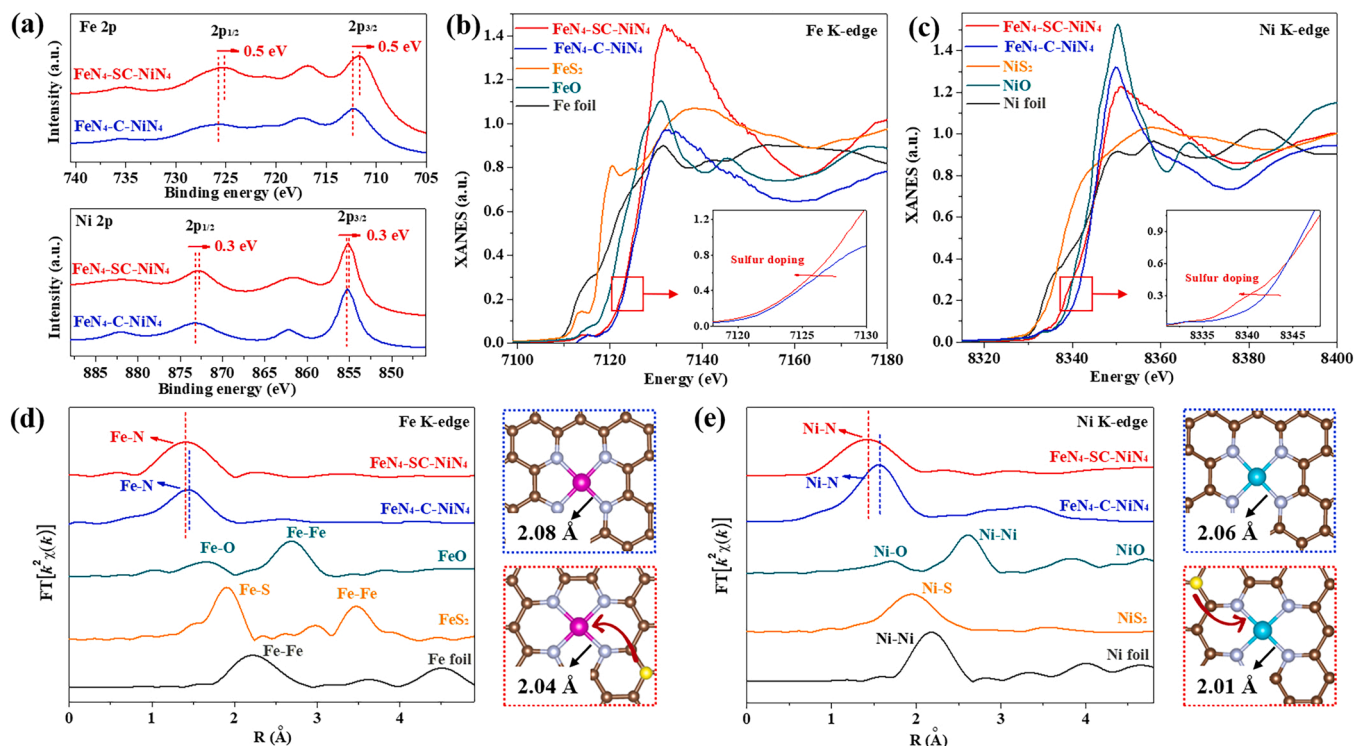


**Fig. 3.** Atomic structure analysis of FeN<sub>4</sub>-SC-NiN<sub>4</sub> and FeN<sub>4</sub>-C-NiN<sub>4</sub>. (a) High-resolution XPS survey at Fe 2p and Ni 2p region. (b, c) XANES spectra, (d, e) FT-EXAFS fitting curves, and optimized configurations at Fe K-edge and Ni K-edge, respectively.

However, the intensity maximum of Fe K-edge and Ni K-edge in FeN<sub>4</sub>-SC-NiN<sub>4</sub> (4.21 Å<sup>-1</sup>, 3.28 Å<sup>-1</sup>) are slightly lower than those in FeN<sub>4</sub>-C-NiN<sub>4</sub>, further verifying the variation of atomic configurations after sulfur doping.

### 3.3. Electrochemical performance

The ORR and OER performance of FeN<sub>4</sub>-SC-NiN<sub>4</sub> were examined by rotating disk electrode (RDE) measurements in O<sub>2</sub>-saturated 0.1 M KOH, in comparison with FeN<sub>4</sub>-C-NiN<sub>4</sub> and mono-component FeN<sub>4</sub>-SC and NiN<sub>4</sub>-SC (the structures were detected by XRD, HRTEM image, AC-HADDF-STEM and EDX mapping in Fig. S18 and S19). As LSV curves shown in Fig. 4a, the FeN<sub>4</sub>-SC-NiN<sub>4</sub> dual-atom sites exhibit the most positive onset ( $E_{\text{onset}} = 0.979$  V) and half-wave potential ( $E_{1/2} = 0.844$  V), which are similar to those of the FeN<sub>4</sub>-SC (1.016, 0.852 V) and much better than FeN<sub>4</sub>-C-NiN<sub>4</sub> (0.957, 0.780 V), and NiN<sub>4</sub>-SC (0.887, 0.720 V). As the trend listed in Fig. 4b, the ORR activity follows the order of FeN<sub>4</sub>-SC-NiN<sub>4</sub>  $\approx$  FeN<sub>4</sub>-SC > Pt/C > FeN<sub>4</sub>-C-NiN<sub>4</sub> > NiN<sub>4</sub>-SC. The corresponding Tafel slope of FeN<sub>4</sub>-SC-NiN<sub>4</sub> shows a value of 84.49 mV dec<sup>-1</sup>, illustrating the superior ORR kinetics (Fig. S20a). Moreover, the ORR performance of FeN<sub>4</sub>-SC-NiN<sub>4</sub> outperforms most of the reported nonprecious catalysts, as listed in Table S4. The OER polarization curves are displayed in Fig. 4c, to reach a current density of 10 mA cm<sup>-2</sup>, the FeN<sub>4</sub>-SC-NiN<sub>4</sub> requires a  $\eta$  of 246 mV, which is similar to NiN<sub>4</sub>-SC (272 mV) and much lower than FeN<sub>4</sub>-C-NiN<sub>4</sub> (332 mV), RuO<sub>2</sub> (359 mV), and FeN<sub>4</sub>-SC (401 mV). As trend shown in Fig. 4d, the OER activity follows the order of FeN<sub>4</sub>-SC-NiN<sub>4</sub>  $\approx$  NiN<sub>4</sub>-SC > FeN<sub>4</sub>-C-NiN<sub>4</sub> > RuO<sub>2</sub> > FeN<sub>4</sub>-SC, which is antipodal to the ORR. The OER Tafel slope of FeN<sub>4</sub>-SC-NiN<sub>4</sub> (74.02 mV dec<sup>-1</sup>) is much lower than that of the RuO<sub>2</sub> (100.66 mV dec<sup>-1</sup>), revealing its favorable OER kinetics (Fig. S20b). Moreover, the OER performance of FeN<sub>4</sub>-SC-NiN<sub>4</sub> outperforms most of the state-of-art non-precious catalysts, as listed in Table S5. Overall, above results indicate the high ORR activity but poor OER activity for FeN<sub>4</sub>-SC, and the high OER activity but poor ORR activity for NiN<sub>4</sub>-SC. This illustrates that the superior oxygen catalytic

activity of FeN<sub>4</sub>-SC-NiN<sub>4</sub> is originated from the separated FeN<sub>4</sub> and NiN<sub>4</sub> sites, which are dominating active sites for ORR and OER, respectively. Meanwhile, the FeN<sub>4</sub>-SC-NiN<sub>4</sub> dual-atom sites exhibit simultaneously enhanced ORR and OER activity in comparison with FeN<sub>4</sub>-C-NiN<sub>4</sub>, indicating the “one stone two birds” bidirectional regulation capacity of sulfur. Furthermore, the ORR performance of FeN<sub>4</sub>-SC and FeN<sub>4</sub>-C, the OER performance of NiN<sub>4</sub>-SC and NiN<sub>4</sub>-C were taken into comparison (Fig. S21). Both the FeN<sub>4</sub>-SC and NiN<sub>4</sub>-SC exhibit remarkably enhanced ORR and OER activity in comparison with the samples without S doping, indicating the crucial role of S for enhancing the ORR activity of FeN<sub>4</sub> and the OER activity of NiN<sub>4</sub>, respectively. As a result, the overall polarization curve of FeN<sub>4</sub>-SC-NiN<sub>4</sub> affords an ultra-small voltage gap ( $\Delta E$ ) of 0.632 V, outperforming the FeN<sub>4</sub>-C-NiN<sub>4</sub> (0.783 V), benchmarked Pt/C+RuO<sub>2</sub> (0.771 V), and most of the state-of-art bifunctional catalysts (Fig. 4e-f).

For comparison, the ORR and OER performance of pure S-doped hollow carbon spheres without metal doping was tested, which exhibit significantly degenerative ORR and OER activity (Fig. S22). This reveals the inactivity of hollow S-doped carbon spheres in FeN<sub>4</sub>-SC-NiN<sub>4</sub>, verifying the pivotal roles of Fe-N<sub>4</sub> and Ni-N<sub>4</sub> as main active sites for ORR and OER. Moreover, the S-doped FeNi particles synthesized without using SiO<sub>2</sub> template exhibit rapidly decayed ORR and OER activity in comparison with FeN<sub>4</sub>-SC-NiN<sub>4</sub>, illustrating that downscaling Fe and Ni sites into atomic level is critical for enhancing both ORR and OER activity (Fig. S23). The oxygen catalytic stability of FeN<sub>4</sub>-SC-NiN<sub>4</sub> was evaluated by ADTs (Fig. 4g). After 5000 continuous cycles, there was almost no decay in terms of  $E_{1/2}$  (5 mV) for ORR and  $\eta_{10}$  (9 mV) for OER, suggesting the remarkable long-term stability of the FeN<sub>4</sub>-SC-NiN<sub>4</sub>. Similarly, the FeN<sub>4</sub>-SC and NiN<sub>4</sub>-SC also exhibited feeble activity decay after ADTs for 5000 continuous cycles, further confirming their superior electrochemical stability (Fig. S24).

The practicability of FeN<sub>4</sub>-SC-NiN<sub>4</sub> was evaluated by assembled into the Zn-air battery operated in 6 M KOH electrolyte, and in comparison with the commercial Pt/C+RuO<sub>2</sub> air-cathode (Fig. S25). As shown in Fig. 4h, the FeN<sub>4</sub>-SC-NiN<sub>4</sub>-based battery exhibits an initial charge

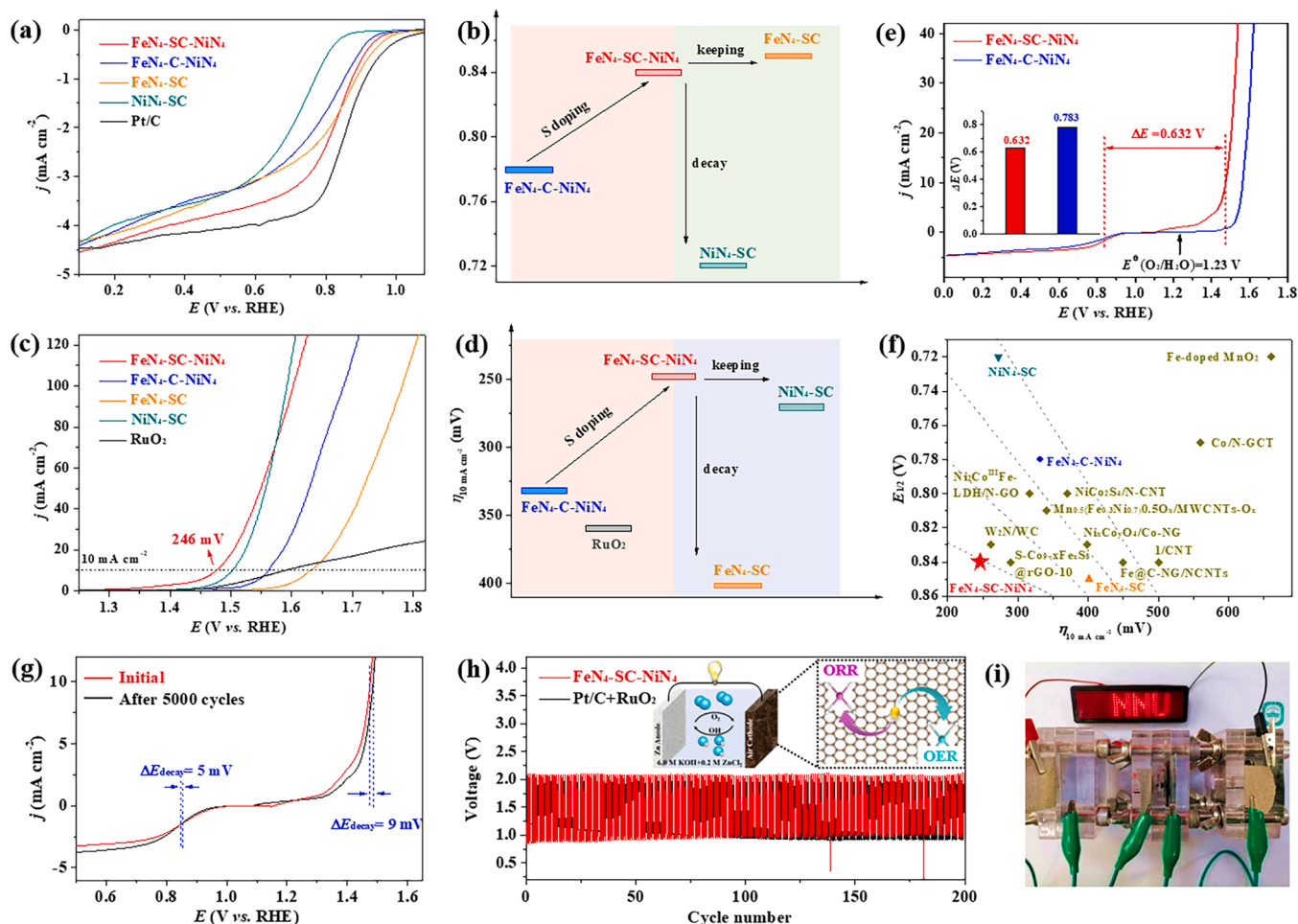


**Fig. 4.** ORR and OER performance of FeN<sub>4</sub>-SC-NiN<sub>4</sub> in 0.1 M KOH. (a) ORR polarization curves and (b) histogram of the  $E_{1/2}$ . (c) OER polarization curves and (d) histogram of the  $\eta_{10}^{-2}$  mA cm<sup>-2</sup>. (e) Overall polarization curve. (f) Oxygen catalytic bifunctionality in comparison with state-of-art catalysts. (g) Durability evolution. (h) Discharge and charge voltage profiles of Zn-air battery at 5 mA cm<sup>-2</sup>. (i) Photo of LED illumination powered by ZAB-FeN<sub>4</sub>-SC-NiN<sub>4</sub>.

potential of 2.05 V and a discharge potential of 0.90 V, delivering a small charge-discharge voltage gap of 1.15 V @ 5 mA cm<sup>-2</sup>. After 200 cycles (~ 67 h), the FeN<sub>4</sub>-SC-NiN<sub>4</sub> air-cathode shows an even better voltage gap to 1.08 V, while the Pt/C+RuO<sub>2</sub> air-cathode shows an obvious decay of 31.13% after 200 cycles. Moreover, the FeN<sub>4</sub>-SC-NiN<sub>4</sub>-assembled Zn-air battery could drive the LED light array for more than 24 h, further confirming the practicality of FeN<sub>4</sub>-SC-NiN<sub>4</sub> (Fig. 4i).

### 3.4. Electrocatalytic mechanisms

DFT calculations were carried out to theoretically identify the dominate ORR and OER active sites in FeN<sub>4</sub>-SC-NiN<sub>4</sub>, and then unravel the bidirectional regulation mechanism of sulfur. The Gibbs free energy profiles for the ORR ( $U=0$  V) were considered at the FeN<sub>4</sub> and NiN<sub>4</sub> sites of FeN<sub>4</sub>-SC-NiN<sub>4</sub>, respectively, as shown in Fig. 5a and Fig. S26. Obviously, in FeN<sub>4</sub>-SC-NiN<sub>4</sub>, the FeN<sub>4</sub> site exhibits more significantly exothermic proton-electron transfer pathway than NiN<sub>4</sub> site, indicating that the FeN<sub>4</sub> site is more active for ORR than NiN<sub>4</sub> site. Other side, the free energy profiles for the OER were considered at the FeN<sub>4</sub> and NiN<sub>4</sub> sites of FeN<sub>4</sub>-SC-NiN<sub>4</sub>, respectively (Fig. 5b). It has been well recognized that the free energy difference between  $G_{OOH^*}$  and  $G_{OH^*}$  is a key reaction descriptor to evaluate OER activity, with an ideal value of 2.46 eV [55]. Thus, the NiN<sub>4</sub> site in FeN<sub>4</sub>-SC-NiN<sub>4</sub> is identified to be more active for OER than FeN<sub>4</sub> site, due to its  $G_{OOH^*}-G_{OH^*}$  much closer to 2.46 eV (2.59 eV vs. 2.93 eV). Overall, the superior oxygen catalytic bifunctionality of FeN<sub>4</sub>-SC-NiN<sub>4</sub> could be originated from the separated FeN<sub>4</sub>

and NiN<sub>4</sub> sites, which enable high ORR and OER activity, respectively.

To shed light on the role of sulfur doping, the ORR and OER pathways of FeN<sub>4</sub>-SC-NiN<sub>4</sub> and S-free FeN<sub>4</sub>-C-NiN<sub>4</sub> were compared. For ORR, as shown in Fig. 5c, the rate determine step (RDS) for both the FeN<sub>4</sub>-SC-NiN<sub>4</sub> and FeN<sub>4</sub>-C-NiN<sub>4</sub> is the OH<sup>\*</sup> desorption, implying that the last step dominates the ORR overpotential [56]. After introducing sulfur into FeN<sub>4</sub>-C-NiN<sub>4</sub>, the energy barrier of OH<sup>\*</sup> desorption is decreased from -0.55 eV to -0.61 eV, indicative a faster ORR kinetics after sulfur doping. For OER, as shown in Fig. 5d, the  $G_{OOH^*}-G_{OH^*}$  of FeN<sub>4</sub>-SC-NiN<sub>4</sub> is much closer to 2.46 eV than that of FeN<sub>4</sub>-C-NiN<sub>4</sub> (2.59 eV vs. 2.84 eV), suggesting the optimized OER pathway after sulfur doping. In order to verify the structural rationality of FeN<sub>4</sub>-SC-NiN<sub>4</sub> model, the FeN<sub>4</sub>-SC-NiN<sub>4</sub>S structure, with sulfur dopants on the same surface of FeN<sub>4</sub> and NiN<sub>4</sub>, was constructed to make a comparison (Fig. S27). Firstly, the thermodynamic stability of FeN<sub>4</sub>-SC-NiN<sub>4</sub> and FeN<sub>4</sub>-SC-NiN<sub>4</sub>S were compared, as shown in Fig. S28. It can be seen that the FeN<sub>4</sub>-SC-NiN<sub>4</sub> structure is thermodynamically more favorable. Secondly, the Gibbs free energy profiles of ORR and OER on FeN<sub>4</sub>-SC-NiN<sub>4</sub> and FeN<sub>4</sub>-SC-NiN<sub>4</sub>S were taken into comparison, as shown in Fig. S29. Obviously, both the ORR and OER were more favorable on FeN<sub>4</sub>-SC-NiN<sub>4</sub>, suggesting that the FeN<sub>4</sub>-SC-NiN<sub>4</sub> could be the best model for DFT calculations.

Combining with the electronic properties analyzed in Fig. 1, the bidirectional regulation mechanism of sulfur could be unveiled. One side for FeN<sub>4</sub> site, the doping of sulfur reduces the Bader charge of Fe site from +1.28 |e| to +1.24 |e|, resulting in a lower spin state of Fe, as quantitatively determined by the decreased magnetic moment from 1.92



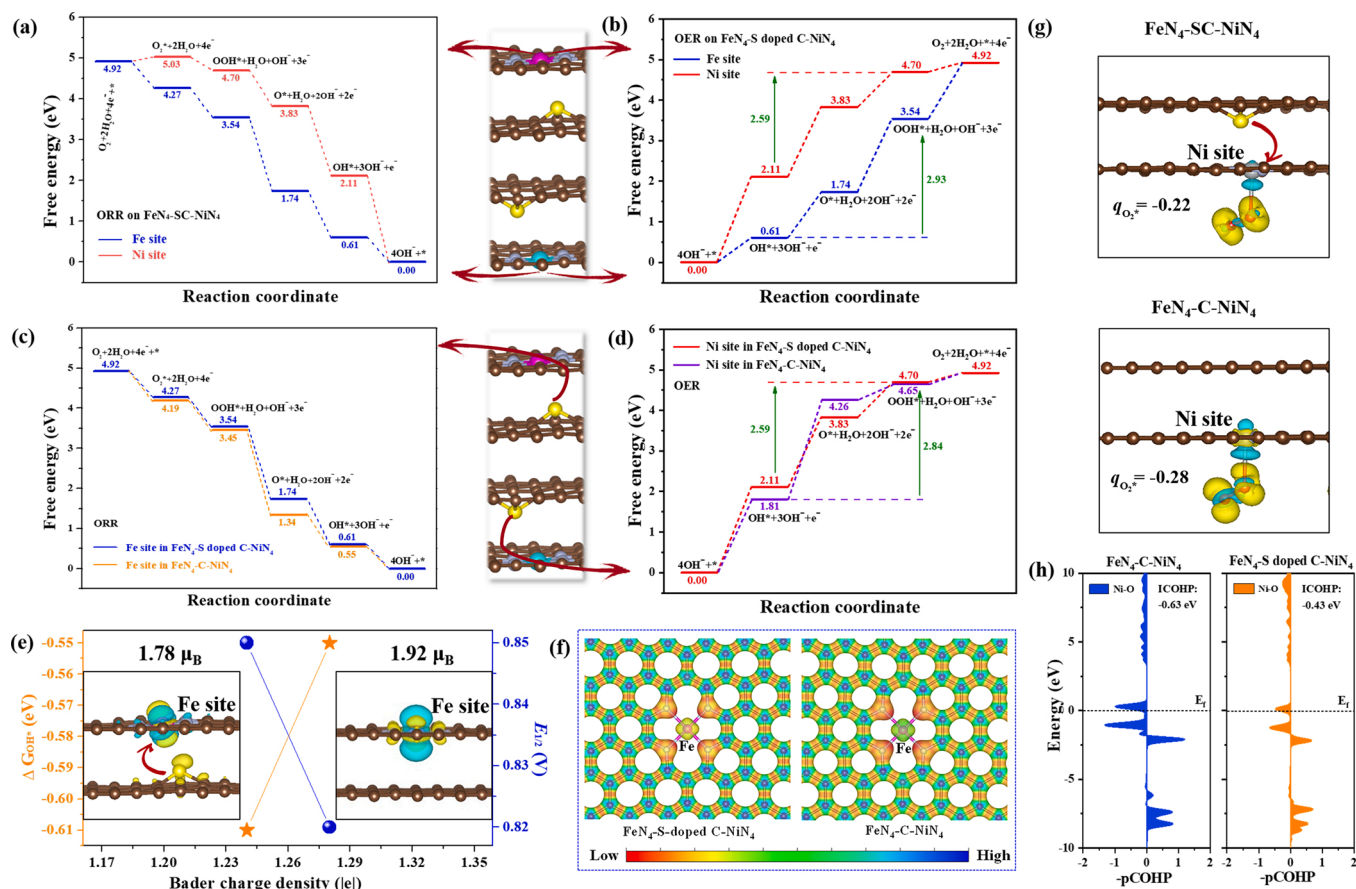


**Fig. 5.** (a, b) Gibbs free energy profiles to identify the ORR and OER active sites in FeN<sub>4</sub>-SC-NiN<sub>4</sub> (U = 0 V). (c, d) Comparison of Gibbs free energies of ORR and OER pathway on FeN<sub>4</sub>-SC-NiN<sub>4</sub> and FeN<sub>4</sub>-C-NiN<sub>4</sub>. (e) Correlations of the magnetic moment of Fe with ΔG<sub>OH\*</sub> and E<sub>1/2</sub> for ORR, inset: spin charge density of Fe site. (f) Electrostatic potential isosurfaces. The blue and red color represents a high/positive and low/negative electrostatic potential value, respectively. (g) Charge density difference of O<sub>2</sub> \* adsorption and (h) COHP analysis of Ni-O bond at Ni site.

to 1.78 μ<sub>B</sub> (Fig. 5e). Such lower spin state leads to a decreased electrostatic potential value (Fig. 5f), weakening the electrostatic interaction with negatively charged OH<sup>-</sup>, thus accelerating the last-step desorption and enhance the ORR activity. The other side for NiN<sub>4</sub> site, the introduction of sulfur largely downshifts the d-band center of Ni from -1.89 eV to -2.13 eV, which is far away from the Fermi level. According to the d-band model theory [57], a lower d-band center value corresponds to a weaker binding ability for surface adsorbed O<sub>2</sub> \*, thus the O<sub>2</sub> \* desorption is facilitated at S-doped NiN<sub>4</sub> site. As verified by charge density difference in Fig. 5g, it indicates a weaker interaction between O<sub>2</sub> and S-doped NiN<sub>4</sub> site, beneficial for the forward OER kinetics. Moreover, the crystal orbital Hamilton populations (COHP) show a higher COHP value (-0.43) at S-doped NiN<sub>4</sub> site, suggesting a weaker Ni-O binding strength for O<sub>2</sub> desorption at last step of OER (Fig. 5h). Based on above analysis, we can get the conclusion that the ambient sulfur mainly reduces the charges for FeN<sub>4</sub> sites while downshifts the d-band center for NiN<sub>4</sub> sites, which directionally promoted the OH\* desorption at FeN<sub>4</sub> sites but accelerated the O<sub>2</sub> \* stripping at NiN<sub>4</sub> sites, making the separated FeN<sub>4</sub> and NiN<sub>4</sub> sites in FeN<sub>4</sub>-SC-NiN<sub>4</sub> more favorable for ORR and OER, respectively.

#### 4. Conclusions

In summary, we have innovatively utilized the L-Methionine biomaterial to fabricate FeN<sub>4</sub>-SC-NiN<sub>4</sub> dual-atom catalyst and verified the anisotropic regulation mechanism of sulfur on severally customizing the electronic states of FeN<sub>4</sub> and NiN<sub>4</sub> sites. By employing FeN<sub>4</sub>-C-NiN<sub>4</sub>, NiN<sub>4</sub>-SC, and FeN<sub>4</sub>-SC as references, we established the relationship

between electronic property and adsorption strength for O<sub>2</sub> \*/OH\*, thus built “one stone two birds” bidirectional regulation mechanism for reversible oxygen electrocatalysis. This work provides a viable approach to enhance the catalytic activity and selectivity of dual-atom catalysts, which is promising for simultaneously promoting multi-catalytic reactions in one system.

#### CRediT authorship contribution statement

**Keying Su:** Methodology, Investigation, Validation, Writing – original draft, Writing – review & editing. **Shan Yang:** Methodology, Investigation. **Anzhou Yang:** Formal analysis, Methodology. **Yi Guo:** Methodology, Investigation. **Bing Liu:** DFT calculation, Funding acquisition. **Jiawei Zhu:** Writing, Funding acquisition. **Yawen Tang:** Resources, Funding acquisition. **Xiaoyu Qiu:** Supervision, Writing – review & editing, Project administration.

#### Declaration of Competing Interest

The authors declare that they have no known competing financial interests or personal relationships that could have appeared to influence the work reported in this paper.

#### Data Availability

Data will be made available on request.

## Acknowledgements

X.Q. acknowledges the financial supports from National Natural Science Foundation of China (21902078). Y.T. acknowledges the financial supports from National Natural Science Foundation of China (21875112). B.L. acknowledges the financial supports from National Natural Science Foundation of China (21802054), and Natural Science Foundation of Jiangsu Province (BK20180587). J. Z. acknowledges the financial supports from National Natural Science Foundation of China (52102258) and Natural Science Foundation of Jiangsu Province (BK20210447). We also acknowledge the supports from National and Local Joint Engineering Research Centre of Biomedical Functional Materials and a project sponsored by the Priority Academic Program Development of Jiangsu Higher Education Institutions.

## Appendix A. Supporting information

Supplementary data associated with this article can be found in the online version at [doi:10.1016/j.apcatb.2023.122694](https://doi.org/10.1016/j.apcatb.2023.122694).

## References

- [1] C. Chen, X.-T. Wang, J.-H. Zhong, J. Liu, G.I.N. Waterhouse, Z.-Q. Liu, Epitaxially grown heterostructured  $\text{SrMnO}_6-x\text{-SrMnO}_3$  with high-valence  $\text{Mn}^{3+/4+}$  for improved oxygen reduction catalysis, *Angew. Chem. Int. Ed.* 60 (2021) 22043–22050, <https://doi.org/10.1002/anie.202109207>.
- [2] Y.-P. Deng, Y. Jiang, R. Liang, S.-J. Zhang, D. Luo, Y. Hu, X. Wang, J.-T. Li, A. Yu, Z. Chen, Dynamic electrocatalyst with current-driven oxyhydroxide shell for rechargeable zinc-air battery, *Nat. Commun.* 11 (2020) 1952, <https://doi.org/10.1038/s41467-020-15853-1>.
- [3] W. Sun, F. Wang, B. Zhang, M. Zhang, V. Küpers, X. Ji, C. Theile, P. Bieker, K. Xu, C. Wang, M. Winter, A rechargeable zinc-air battery based on zinc peroxide chemistry, *Science* 371 (2021) 46–51, <https://doi.org/10.1126/science.abb9554>.
- [4] J. Yin, J. Jin, H. Liu, B. Huang, M. Lu, J. Li, H. Liu, H. Zhang, Y. Peng, P. Xi, C.-H. Yan,  $\text{NiCo}_2\text{O}_4$ -based nanosheets with uniform 4 nm mesopores for excellent Zn-Air battery performance, *Adv. Mater.* 32 (2020) 2001651, <https://doi.org/10.1002/adma.202001651>.
- [5] Z. Liang, N. Kong, C. Yang, W. Zhang, H. Zheng, H. Lin, R. Cao, Highly curved nanostructure-coated Co, N-doped carbon materials for oxygen electrocatalysis, *Angew. Chem. Int. Ed.* 60 (2021) 12759–12764, <https://doi.org/10.1002/anie.202101562>.
- [6] Y. Jiang, Y.-P. Deng, R. Liang, J. Fu, R. Gao, D. Luo, Z. Bai, Y. Hu, A. Yu, Z. Chen, d-Orbital steered active sites through ligand editing on heterometal imidazole frameworks for rechargeable zinc-air battery, *Nat. Commun.* 11 (2020) 5858, <https://doi.org/10.1038/s41467-020-19709-6>.
- [7] Z. Wang, J. Huang, L. Wang, Y. Liu, W. Liu, S. Zhao, Z.-Q. Liu, Cation-tuning induced d-band center modulation on co-based spinel oxide for rechargeable Zn-air batteries, *Angew. Chem. Int. Ed.* 61 (2022), e202114696, <https://doi.org/10.1002/anie.202114696>.
- [8] X. Hu, Y. Min, L.-L. Ma, J.-Y. Lu, H.-C. Li, W.-J. Liu, J.-J. Chen, H.-Q. Yu, Iron-nitrogen doped carbon with exclusive presence of  $\text{Fe}_x\text{N}$  active sites as an efficient ORR electrocatalyst for Zn-air battery, *Appl. Catal. B Environ.* 268 (2020), 118405, <https://doi.org/10.1016/j.apcatb.2019.118405>.
- [9] Y. Chen, R. Gao, S. Ji, H. Li, K. Tang, P. Jiang, H. Hu, Z. Zhang, H. Hao, Q. Qu, X. Liang, W. Chen, J. Dong, D. Wang, Y. Li, Atomic-level modulation of electronic density at cobalt single-atom sites derived from metal-organic frameworks: enhanced oxygen reduction performance, *Angew. Chem. Int. Ed.* 60 (2021) 3212–3221, <https://doi.org/10.1002/anie.202012798>.
- [10] T. Cui, Y.-P. Wang, T. Ye, J. Wu, Z. Chen, J. Li, Y. Lei, D. Wang, Y. Li, Engineering Dual Single-Atom Sites on 2D ultrathin N-doped carbon nanosheets attaining ultra-low-temperature zinc-air battery, *Angew. Chem. Int. Ed.* 61 (2022), e202115219, <https://doi.org/10.1002/anie.202115219>.
- [11] A. Saad, D. Liu, Y. Wu, Z. Song, Y. Li, T. Najam, K. Zong, P. Tsiakaras, X. Cai, Ag nanoparticles modified crumpled borophene supported  $\text{Co}_3\text{O}_4$  catalyst showing superior oxygen evolution reaction (OER) performance, *Appl. Catal. B Environ.* 298 (2021), 120529, <https://doi.org/10.1016/j.apcatb.2021.120529>.
- [12] J. Qi, Y.-P. Lin, D. Chen, T. Zhou, W. Zhang, R. Cao, Autologous cobalt phosphates with coordinated coordination sites for electrocatalytic water oxidation, *Angew. Chem. Int. Ed.* 59 (2020) 8917–8921, <https://doi.org/10.1002/anie.202001737>.
- [13] X.-T. Wang, T. Ouyang, L. Wang, J.-H. Zhong, Z.-Q. Liu, Surface reorganization on electrochemically-induced Zn-Ni-Co spinel oxides for enhanced oxygen electrocatalysis, *Angew. Chem. Int. Ed.* 59 (2020) 6492–6499, <https://doi.org/10.1002/anie.202000690>.
- [14] P. Peng, L. Shi, F. Huo, C. Mi, X. Wu, S. Zhang, Z. Xiang, A pyrolysis-free path toward superiorly catalytic nitrogen-coordinated single atom, *Sci. Adv.* 5 (2019) eaaw2322, <https://doi.org/10.1126/sciadv.aaw2322>.
- [15] D. Chen, J. Zhu, X. Mu, R. Cheng, W. Li, S. Liu, Z. Pu, C. Lin, S. Mu, Nitrogen-Doped carbon coupled  $\text{FeNi}_3$  intermetallic compound as advanced bifunctional electrocatalyst for OER, ORR and Zn-air batteries, *Appl. Catal. B Environ.* 268 (2020), 118729, <https://doi.org/10.1016/j.apcatb.2020.118729>.
- [16] B. Wei, Z. Fu, D. Legut, T.C. Germann, S. Du, H. Zhang, J.S. Francisco, R. Zhang, Rational design of highly stable and active MXene-based bifunctional ORR/OER double-atom catalysts, *Adv. Mater.* 33 (2021) 2102595, <https://doi.org/10.1002/adma.202102595>.
- [17] G. Yang, J. Zhu, P. Yuan, Y. Hu, G. Qu, B.-A. Lu, X. Xue, H. Yin, W. Cheng, J. Cheng, W. Xu, J. Li, J. Hu, S. Mu, J.-N. Zhang, Regulating Fe-spin state by atomically dispersed Mn-N in Fe-N-C catalysts with high oxygen reduction activity, *Nat. Commun.* 12 (2021) 1734, <https://doi.org/10.1038/s41467-021-21919-5>.
- [18] Z. Chen, X. Su, J. Ding, N. Yang, W. Zuo, Q. He, Z. Wei, Q. Zhang, J. Huang, Y. Zhai, Boosting oxygen reduction reaction with Fe and Se dual-atom sites supported by nitrogen-doped porous carbon, *Appl. Catal. B Environ.* 308 (2022), 121206, <https://doi.org/10.1016/j.apcatb.2022.121206>.
- [19] Z. Tan, M. Haneda, H. Kitagawa, B. Huang, Slow synthesis methodology-directed immiscible octahedral  $\text{Pd}_x\text{Rh}_{1-x}$  dual-atom-site catalysts for superior three-way catalytic activities over Rh, *Angew. Chem. Int. Ed.* 61 (2022) 202202588, <https://doi.org/10.1002/anie.202202588>.
- [20] X. Han, X. Ling, D. Yu, D. Xie, L. Li, S. Peng, C. Zhong, N. Zhao, Y. Deng, W. Hu, Atomically dispersed binary Co-Ni sites in nitrogen-doped hollow carbon nanocubes for reversible oxygen reduction and evolution, *Adv. Mater.* 31 (2019) 1905622, <https://doi.org/10.1002/adma.201905622>.
- [21] M. Liu, N. Li, S. Cao, X. Wang, X. Lu, L. Kong, Y. Xu, X.-H. Bu, A "pre-constrained metal twins" strategy to prepare efficient dual-metal-atom catalysts for cooperative oxygen electrocatalysis, *Adv. Mater.* 34 (2022) 2107421, <https://doi.org/10.1002/adma.202107421>.
- [22] C. Wang, K. Wang, Y. Feng, C. Li, X. Zhou, L. Gan, Y. Feng, H. Zhou, B. Zhang, X. Qu, H. Li, J. Li, A. Li, Y. Sun, S. Zhang, G. Yang, Y. Guo, S. Yang, T. Zhou, F. Dong, K. Zheng, L. Wang, J. Huang, Z. Zhang, X. Han, Co and Pt dual-single-atoms with oxygen-coordinated Co-O-Pt dimer sites for ultrahigh photocatalytic hydrogen evolution efficiency, *Adv. Mater.* 33 (2021) 2003327, <https://doi.org/10.1002/adma.202003327>.
- [23] H. Peng, F. Liu, X. Liu, S. Liao, C. You, X. Tian, H. Nan, F. Luo, H. Song, Z. Fu, P. Huang, Effect of transition metals on the structure and performance of the doped carbon catalysts derived from polyaniline and melamine for ORR application, *ACS Catal.* 4 (2014) 3797–3805, <https://doi.org/10.1021/cs500744x>.
- [24] X.X. Wang, D.A. Cullen, Y.-T. Pan, S. Hwang, M. Wang, Z. Feng, J. Wang, M. H. Engelhard, H. Zhang, Y. He, Y. Shao, D. Su, K.L. More, J.S. Spendlow, G. Wu, Nitrogen-coordinated single cobalt atom catalysts for oxygen reduction in proton exchange membrane fuel cells, *Adv. Mater.* 30 (2018) 1706758, <https://doi.org/10.1002/adma.201706758>.
- [25] H. Fei, J. Dong, Y. Feng, C.S. Allen, C. Wan, B. Voloskiy, M. Li, Z. Zhao, Y. Wang, H. Sun, P. An, W. Chen, Z. Guo, C. Lee, D. Chen, I. Shakir, M. Liu, T. Hu, Y. Li, Angus I. Kirkland, X. Duan, Y. Huang, General synthesis and definitive structural identification of  $\text{MN}_4\text{C}_4$  single-atom catalysts with tunable electrocatalytic activities, *Nat. Catal.* 1 (2018) 63–72, <https://doi.org/10.1038/s41929-017-0008-y>.
- [26] R. Subbaraman, D. Tripkovic, K.-C. Chang, D. Strmcnik, A.P. Paulikas, P. Hirunsit, M. Chan, J. Greeley, V. Stamenkovic, N.M. Markovic, Trends in activity for the water electrolyser reactions on 3d M (Ni, Co, Fe, Mn) hydr(oxy)oxide catalysts, *Nat. Mater.* 11 (2012) 550–557, <https://www.nature.com/articles/nmat3131>.
- [27] Z. Zhu, H. Yin, Y. Wang, C.-H. Chuang, L. Xing, M. Dong, Y.-R. Lu, G. Casillas-Garcia, Y. Zheng, S. Chen, Y. Dou, P. Liu, Q. Cheng, H. Zhao, Coexisting single-atomic Fe and Ni sites on hierarchically ordered porous carbon as a highly efficient ORR electrocatalyst, *Adv. Mater.* 32 (2020) 2004670, <https://doi.org/10.1002/adma.202004670>.
- [28] M. Ma, A. Kumar, D. Wang, Y. Wang, Y. Jia, Y. Zhang, G. Zhang, Z. Yan, X. Sun, Boosting the bifunctional oxygen electrocatalytic performance of atomically dispersed Fe site via atomic Ni neighboring, *Appl. Catal. B Environ.* 274 (2020), 119091, <https://doi.org/10.1016/j.apcatb.2020.119091>.
- [29] J. Chen, H. Li, C. Fan, Q. Meng, Y. Tang, X. Qiu, G. Fu, T. Ma, Dual single-atomic Ni-N<sub>4</sub> and Fe-N<sub>4</sub> sites constructing janus hollow graphene for selective oxygen electrocatalysis, *Adv. Mater.* 32 (2020) 2003134, <https://doi.org/10.1002/adma.202003134>.
- [30] X. Zhao, F. Wang, X.-P. Kong, R. Fang, Y. Li, Dual-metal hetero-single-atoms with different coordination for efficient synergistic catalysis, *J. Am. Chem. Soc.* 143 (2021) 16068–16077, <https://doi.org/10.1021/jacs.1c06349>.
- [31] Y. Zhao, H. Zhou, X. Zhu, Y. Qu, C. Xiong, Z. Xue, Q. Zhang, X. Liu, F. Zhou, X. Mou, W. Wang, M. Chen, Y. Xiong, X. Lin, Y. Lin, W. Chen, H.-J. Wang, Z. Jiang, L. Zheng, T. Yao, J. Dong, S. Wei, W. Huang, L. Gu, J. Luo, Y. Li, Y. Wu, Simultaneous oxidative and reductive reactions in one system by atomic design, *Nat. Catal.* 4 (2021) 134–143, <https://doi.org/10.1038/s41929-020-00563-0>.
- [32] Q. Li, W. Chen, H. Xiao, Y. Gong, Z. Li, L. Zheng, X. Zheng, W. Yan, W.-C. Cheong, R. Shen, N. Fu, L. Gu, Z. Zhuang, C. Chen, D. Wang, Q. Peng, J. Li, Y. Li, Fe isolated single atoms on S, N codoped carbon by copolymer pyrolysis strategy for highly efficient oxygen reduction reaction, *Adv. Mater.* 30 (2018) 1800588, <https://doi.org/10.1002/adma.201800588>.
- [33] H. Shen, E. Gracia-Espino, J. Ma, K. Zang, J. Luo, L. Wang, S. Gao, X. Mamat, G. Hu, T. Wagberg, Synergistic effects between atomically dispersed Fe-N-C and C-S-C for the oxygen reduction reaction in acidic media, *Angew. Chem. Int. Ed.* 56 (2017) 13800–13804, <https://doi.org/10.1002/anie.201706602>.
- [34] H. Shang, X. Zhou, J. Dong, A. Li, X. Zhao, Q. Liu, Y. Lin, J. Pei, Z. Li, Z. Jiang, D. Zhou, L. Zheng, Y. Wang, J. Zhou, Z. Yang, R. Cao, R. Sarangi, T. Sun, X. Yang, X. Zheng, W. Yan, Z. Zhuang, J. Li, W. Chen, D. Wang, J. Zhang, Y. Li, Engineering unsymmetrically coordinated  $\text{Cu-S}_2\text{N}_3$  single atom sites with enhanced oxygen

- reduction activity, *Nat. Commun.* 11 (2020) 3049, <https://doi.org/10.1038/s41467-020-16848-8>.
- [35] Y. Zhao, N. Yang, H. Yao, D. Liu, L. Song, J. Zhu, S. Li, L. Gu, K. Lin, D. Wang, Stereodefined codoping of sp-N and S atoms in few-layer graphdiyne for oxygen evolution reaction, *J. Am. Chem. Soc.* 141 (2019) 7240–7244, <https://doi.org/10.1021/jacs.8b13695>.
- [36] J. Jin, J. Yin, H. Liu, B. Huang, Y. Hu, H. Zhang, M. Sun, Y. Peng, P. Xi, C.-H. Yan, Atomic sulfur filling oxygen vacancies optimizes H absorption and boosts the hydrogen evolution reaction in alkaline media, *Angew. Chem. Int. Ed.* 60 (2021) 14117–14123, <https://doi.org/10.1002/anie.202104055>.
- [37] Y. Mun, S. Lee, K. Kim, S. Kim, S. Lee, J.W. Han, J. Lee, Versatile strategy for tuning ORR activity of a single Fe-N<sub>4</sub> site by controlling electron-withdrawing/donating properties of a carbon plane, *J. Am. Chem. Soc.* 141 (2019) 6254–6262, <https://doi.org/10.1021/jacs.8b13543>.
- [38] W. Stöber, F. Arthur, B. Ernst, Controlled growth of monodisperse silica spheres in the micron size range, *J. Colloid Interface Sci.* 26 (1968) 62–69, [https://doi.org/10.1016/0021-9797\(68\)90272-5](https://doi.org/10.1016/0021-9797(68)90272-5).
- [39] C. Tang, Y. Liu, C. Xu, J. Zhu, X. Wei, L. Zhou, L. He, W. Yang, L. Mai, Ultrafine nickel-nanoparticle-enabled SiO<sub>2</sub> hierarchical hollow spheres for high-performance lithium storage, *Adv. Funct. Mater.* 28 (2018) 1704561, <https://doi.org/10.1002/adfm.201704561>.
- [40] J. Liang, Q. Song, J. Wu, Q. Lei, J. Li, W. Zhang, Z. Huang, T. Kang, H. Xu, P. Wang, X. Zhou, P.K. Wong, H. Li, X. Meng, Z. Jiang, C.-S. Lee, Anchoring copper single atoms on porous boron nitride nanofiber to boost selective reduction of nitroaromatics, *ACS Nano* 16 (2022) 4152–4161, <https://doi.org/10.1021/acsnano.1c10003>.
- [41] W. Yao, J. Zhang, J. Ji, H. Yang, B. Zhou, X. Chen, P. Boggild, P.U. Jepsen, J. Tang, F. Wang, L. Zhang, J. Liu, B. Wu, J. Dong, Y. Liu, Bottom-up-etching-mediated synthesis of large-scale pure monolayer graphene on cyclic-polishing-annealed Cu (111), *Adv. Mater.* 34 (2022) 2108608, <https://doi.org/10.1002/adma.202108608>.
- [42] J. Sui, H. Liu, S. Hu, K. Sun, G. Wan, H. Zhou, X. Zheng, H.-L. Jiang, A general strategy to immobilize single-atom catalysts in metal-organic frameworks for enhanced photocatalysis, *Adv. Mater.* 34 (2022) 2109203, <https://doi.org/10.1002/adma.202109203>.
- [43] S. Seok, M. Choi, Y. Lee, D. Jang, Y. Shin, Y.-H. Kim, C. Jo, S. Park, Ni nanoparticles on Ni Core/N-doped carbon shell heterostructures for electrocatalytic oxygen evolution, *ACS Appl. Nano Mater.* 4 (2021) 9418–9429, <https://doi.org/10.1021/acsnm.1c01908>.
- [44] F.M. Enunjekwu, Y. Zhang, C.I. Ezech, H. Zhao, M. Xu, H. Do, T. Wu, Insights into the effects of single Mo vacancy sites on the adsorption and dissociation of CO<sub>2</sub> and H<sub>2</sub>O over the tertiary N-doped MoS<sub>2</sub> monolayers, *Appl. Surf. Sci.* 577 (2022), 151908, <https://doi.org/10.1016/j.apsusc.2021.151908>.
- [45] M. Ha, D.Y. Kim, M. Umer, V. Gladkikh, C.W. Myung, K.S. Kim, Tuning metal single atoms embedded in N<sub>x</sub>C<sub>y</sub> moieties toward high-performance electrocatalysis, *Energy Environ. Sci.* 14 (2021) 3455–3468, <https://doi.org/10.1039/D1EE00154J>.
- [46] X. Li, S. Xi, L. Sun, S. Dou, Z. Huang, T. Su, X. Wang, Isolated FeN<sub>4</sub> sites for efficient electrocatalytic CO<sub>2</sub> reduction, *Adv. Sci.* 7 (2020) 2001545, <https://doi.org/10.1002/adv.202001545>.
- [47] G. Chen, Y. An, S. Liu, F. Sun, H. Qi, H. Wu, Y. He, P. Liu, R. Shi, J. Zhang, A. Kuc, U. Kaiser, T. Zhang, T. Heine, G. Wu, X. Feng, Highly accessible and dense surface single metal FeN<sub>4</sub> active sites for promoting the oxygen reduction reaction, *Energy Environ. Sci.* 15 (2022) 2619–2628, <https://doi.org/10.1039/D2EE00542E>.
- [48] Y. Li, N.M. Adli, W. Shan, M. Wang, M.J. Zachman, S. Hwang, H. Tabassum, S. Karakalos, Z. Feng, G. Wang, Y.C. Li, G. Wu, Atomically dispersed single Ni site catalysts for high-efficiency CO<sub>2</sub> electroreduction at industrial-level current densities, *Energy Environ. Sci.* 15 (2022) 2108–2119, <https://doi.org/10.1039/D2EE00318J>.
- [49] Z. Chen, H. Niu, J. Ding, H. Liu, P.H. Chen, Y.H. Lu, Y.R. Lu, W. Zuo, L. Han, Y. Guo, S.F. Hung, Y. Zhai, Unraveling the origin of sulfur-doped Fe-N-C single-atom catalyst for enhanced oxygen reduction activity: effect of iron spin-state tuning, *Angew. Chem. Int. Ed.* 60 (2021) 25404–25410, <https://doi.org/10.1002/anie.202110243>.
- [50] J. Chen, B. Huang, R. Cao, L. Li, X. Tang, B. Wu, Y. Wu, T. Hu, K. Yuan, Y. Chen, Steering local electronic configuration of Fe-N-C-based coupling catalysts via ligand engineering for efficient oxygen electroreduction, *Adv. Funct. Mater.* (2022) 2209315, <https://doi.org/10.1002/adfm.202209315>.
- [51] X. Yang, J. Cheng, H. Lv, X. Yang, L. Ding, Y. Xu, K. Zhang, W. Sun, J. Zhou, Sulfur-doped unsaturated Ni-N<sub>3</sub> coordination for efficient electroreduction of CO<sub>2</sub>, *Chem. Eng. J.* 450 (2022), 137950, <https://doi.org/10.1016/j.cej.2022.137950>.
- [52] S. Chen, X. Li, C.W. Kao, T. Luo, K. Chen, J. Fu, C. Ma, H. Li, M. Li, T.S. Chan, M. Liu, Unveiling the proton-feeding effect in sulfur-doped Fe-N-C single-atom catalyst for enhanced CO<sub>2</sub> electroreduction, *Angew. Chem. Int. Ed.* 61 (2022), e202206233, <https://doi.org/10.1002/anie.202206233>.
- [53] Y. Chen, Z. Li, Y. Zhu, D. Sun, X. Liu, L. Xu, Y. Tang, Atomic Fe dispersed on N-doped carbon hollow nanospheres for high-efficiency electrocatalytic oxygen reduction, *Adv. Mater.* 31 (2019) 1806312, <https://doi.org/10.1002/adma.201806312>.
- [54] J. Zhang, Y. Zhao, C. Chen, Y.-C. Huang, C.-L. Dong, C.-J. Chen, R.-S. Liu, C. Wang, K. Yan, Y. Li, G. Wang, Tuning the coordination environment in single-atom catalysts to achieve highly efficient oxygen reduction reactions, *J. Am. Chem. Soc.* 141 (2019) 20118–20126, <https://doi.org/10.1021/jacs.9b09352>.
- [55] H.-Y. Su, Y. Gorlin, I.C. Man, F. Calle-Vallejo, J.K. Nørskov, T.F. Jaramillo, J. Rossmeisl, Identifying active surface phases for metal oxide electrocatalysts: a study of manganese oxide bi-functional catalysts for oxygen reduction and water oxidation catalysis, *Phys. Chem. Chem. Phys.* 14 (2012) 14010–14022, <https://doi.org/10.1039/C2CP40841D>.
- [56] T. Bligaard, J.K. Nørskov, S. Dahl, J. Matthiesen, C.H. Christensen, J. Sehested, The Brønsted-Evans-Polanyi relation and the volcano curve in heterogeneous catalysis, *J. Catal.* 224 (2004) 206–217, <https://doi.org/10.1016/j.jcat.2004.02.034>.
- [57] B. Hammer, J.K. Nørskov, Why gold is the noblest of all the metals, *Nature* 376 (1995) 238–240, <https://www.nature.com/articles/376238a0>.